Journal of Alloys and Compounds 695 (2017) 1223–1230

Contents lists available at ScienceDirect

Journal of Alloys and Compounds

journal homepage: http://www.elsevier.com/locate/jalcom

A high-performance anode material based on $FeMnO_3$/graphene composite

Heng Bin [a], Zhenpeng Yao [b], Shenmin Zhu [a, *], Chengling Zhu [a], Hui Pan [a], Zhixin Chen [c], Chris Wolverton [b], Di Zhang [a]

[a] State Key Laboratory of Metal Matrix Composites, Shanghai Jiao Tong University, 800 Dongchuan Road, Shanghai, 200240, PR China
[b] Department of Materials Science and Engineering, Northwestern University, 2220 Campus Drive, Evanston, IL, 60208, United States
[c] School of Mechanical, Materials & Mechatronics Engineering, University of Wollongong, Wollongong, NSW, 2522, Australia

ARTICLE INFO

Article history:
Received 18 August 2016
Received in revised form
21 October 2016
Accepted 22 October 2016
Available online 27 October 2016

Keywords:
Manganese-based oxide
Anode
Graphene
Li-ion battery
First principles calculations

ABSTRACT

Transition metal oxides are attractive as anode materials in lithium-ion batteries for their high theoretical capacity and good performance. In this work, an anode material based on manganese-based oxide $FeMnO_3$ in LIBs is investigated for the first time. $FeMnO_3$ is prepared with graphene and the $FeMnO_3$/graphene composite exhibits a high discharge capacity of 1155.3 mAh g^{-1} after 300 cycles at 200 mA g^{-1}, as well as a superior rate performance of 851.7 mAh g^{-1} at a current density of 3200 mA g^{-1}. The observed extraordinary performance is believed to be attributed to the combination of the intrinsically high capacity of $FeMnO_3$, a large surface area of 89.65 m^2 g^{-1} and good electrical conductivity of the $FeMnO_3$/graphene composite. To help clarify the properties of this new material, we employ first principles calculations to determine the structural stability, electronic structure, and Li ion diffusivity of $FeMnO_3$. The calculations show that $FeMnO_3$ has a relatively low band gap (an indication of reasonable electrical conductivity) and Li ions exhibit a large room temperature diffusivity in $FeMnO_3$.

1. Introduction

With the rapid development of portable electronic devices and hybrid-electric vehicles, lithium-ion batteries (LIBs) are becoming more and more attractive, due to their high energy density, fast charge/discharge rate and long cycling life [1–3]. Unfortunately, the low theoretical capacity of 372 mAh g^{-1} of commercial graphite anodes is a limit on the overall energy density of the cell. Significant effort has been made in searching for potential substitutes for graphite as the anode material. Transitional metal oxides [4,5], including zinc oxides [6], manganese oxides [7–10], iron oxides [11,12], cobalt oxides [13], and tin oxides [14] have demonstrated excellent properties as anode materials in LIBs. Among them, manganese oxides and related compounds have attracted particular attention. They possess not only high energy capacity and low conversion potential but also some other advantages such as multiple valence states, earth-abundant elements, low toxicity and cost. For example, Mn_2O_3 with diverse morphologies has been reported to show a reversible discharge capacity of 470.3 mAh g^{-1} at a current density of 3200 mA g^{-1} after 100 cycles [8]. Generally speaking, metal oxides have poor electrical conductivity, but this can be improved by doping with other elements [15,16]. Therefore the manganese-based ternary oxides may have better performance in LIBs compared with manganese oxides. Bijelić et al. [17] reported that the manganese-based ternary oxide, $CoMn_2O_4$, has a long cycle life with a capacity of 624 mAh g^{-1} after 1000 cycles at 200 mA g^{-1}.

Here, we turn our attention to another manganese-based oxide, $FeMnO_3$, which has previously attracted more attention due to its magnetic properties [18] than its electrochemical properties. $FeMnO_3$ has a bixbyite crystal structure with Fe and Mn ions randomly occupying the 8b and 24d sites with an atom ratio of 1:1 [19]. Here, we demonstrate the synthesis and the performance of $FeMnO_3$ as an anode in LIBs. Furthermore, by combining oxides with active carbon materials in various nanostructural morphologies, one can enhance the electrochemical reaction kinetics and performance [12,20]. For instance, graphene has been used to buffer volume change, anchor active materials and prevent nanostructural oxides from agglomerating during continuous charge/discharge cycles in LIBs [21–23]. Therefore graphene is a good

* Corresponding author.
E-mail address: smzhu@sjtu.edu.cn (S. Zhu).

http://dx.doi.org/10.1016/j.jallcom.2016.10.249
0925-8388/

candidate for the $FeMnO_3$ composite because it has large specific surface area and high electron conductivity.

Herein, a two-step procedure was established for the synthesis of a $FeMnO_3$/graphene composite. When the prepared composite used as an anode in LIBs, it shows very favorable electrochemical properties: a high reversible capacity of 1155.3 mAh g^{-1} after 300 cycles at 200 mA g^{-1} and a good rate performance of 851.7 mAh g^{-1} at a current density of 3200 mA g^{-1}. The electrical conductivity of the $FeMnO_3$ and the diffusivity of Li ion in $FeMnO_3$ were also calculated by using density functional theory (DFT). In the calculations, the Special Quasi-random Structure (SQS) [24] method and ab-initio molecular dynamic simulations were used to determine the disordered structure of $FeMnO_3$, predict the band gap of the disordered bixbyite compound, and determine the temperature-dependent Li ion diffusivity in $FeMnO_3$. The calculations show that $FeMnO_3$ is a low-bandgap semiconductor, with a small band gap of ~0.3 eV (Silicon, 0.75 eV [25]), and the diffusivity of Li ion in $FeMnO_3$ is ~3.9×10^{-12} cm^2 s^{-1} which is comparable to state-of-the-art fast Li-ion conducting electrode materials ($LiMn_2O_4$, ~10^{-11} cm^2 s^{-1} [26] and graphite, 1.12×10^{-10} cm^2 s^{-1} [27]).

2. Experimental

2.1. Synthesis of $FeMnO_3$ and graphene composites

$FeMnO_3$/graphene composite (denoted as FMO-RGO) was synthesized via a two-step procedure. In the first step, 5 mmol of $Mn(COOCH_3)_2 \cdot 4H_2O$ and 5 mmol of $FeCl_3 \cdot 6H_2O$ were dissolved in 20 mL of deionized water under 0.5 h magnetic stirring at room temperature. Then 0.5 mL of ammonia solution was added into the above solution drop by drop under continuously magnetic stirring for 0.5 h which resulted in a brown suspended solution. The brown suspension was collected by centrifugation and washed with deionized water three times before dried at 60 °C for 12 h. Subsequently, the dried product was calcined at 550 °C for 3 h in air and $FeMnO_3$ particles were obtained (denoted as FMO). In the second step, graphene oxide (GO) was prepared from natural graphite flakes using a modified Hummers method. Then 40 mg of the obtained FMO and 17 mg of GO were added into 20 mL of deionized water and the solution was under ultra-sonication treatment for 0.5 h. Afterward, the solution was transferred into a 60 mL Teflon-lined stainless steel autoclave which was heated at 180 °C in an oven for 3 h and then furnace cooled to room temperature. Finally the obtained product was collected through centrifugation, washed with deionized water three times and dried at 60 °C for 6 h in an oven. For a comparison, GO was reduced to RGO in the same hydrothermal process at 180 °C in an oven for 3 h but without the presence of FMO. Then FMO was physically mixed with RGO also at the mass ratio of 7:3 and the mixture is denoted as FMO/RGO MIX. In this investigation the electrochemical performance of the bare FMO was also conducted as a reference.

2.2. Characterization

The obtained samples were characterized by X-ray powder diffraction (XRD) on a RigakuD/max 2550VL/PC system operated at 35 kV and 200 mA with Cu Kα radiation (λ = 1.5406 Å). The atomic ratio of Fe and Mn in FMO was analyzed by using X-ray fluorescence spectrometer (XRF, EDX-720). X-ray photoelectron spectroscopy (XPS) was carried on a physical electronics PHI5400 using Mg Kα radiation as the X-ray source. Raman spectroscopy was performed on a SENTERRA R200 Raman microscope. All the spectra were corrected with C 1s (284.8 eV) band. Nitrogen adsorptions at 77 K were measured on an ASAP2020 volumetric adsorption analyzer. Scanning electron microscopy (SEM) was performed on a JEOLJSM-6360LV field emission microscope at 15 kV. Transmission electron microscopy (TEM) was carried out on a JEOL2010 microscope at 200 kV.

2.3. Electrochemical measurement

Electrochemical experiments were performed on coin-type cells which were assembled in an argon filled glove box (Mikrouna1220/750). The working electrodes were made by mixing the $FeMnO_3$/graphene composite with carbon black and a binder (polyvinylidene fluoride, PVDF) at a mass ratio of 8: 1: 1. The mixture was cast on copper foils of 12 mm in diameter and dried in vacuum at 110 °C for 12 h. A typical loading mass of the active material was 0.8–1.2 mg. Metallic lithium foil was used as the counter electrode and Celgard 2300 microporous membrane was used as the separator. The electrolyte was made of 1 M LiPF6 dissolved in the mixture of ethylene carbonate (EC) and diethylene carbonate (DEC) with the volume ratio of 1: 1. The galvanostatic charge/discharge experiment was carried on a Land CT2001A battery test system in the potential range of 0.01–3.0 V at 25 ± 3 °C. Cyclic voltammetry (CV) curves were acquired on a Chenhua CHI 660D electrochemical workstation in the potential range of 0.01–3.0 V at a scan rate of 0.5 mV s^{-1}. Electrochemical impedance spectroscopy (EIS) was carried out on a Chenhua CHI 660D electrochemical workstation with an AC voltage 5 mV, in the frequencies between 100 kHz and 0.01 Hz. For comparison, the electrochemical performances of the FMO and FMO/RGO MIX electrodes were measured under the same condition.

2.4. Computational methodology

2.4.1. Density functional theory calculations

The first principle calculations were conducted using the Vienna Ab-initio Simulation Package (VASP) [28–31] and the projector augmented wave (PAW) potentials [32]. The generalized gradient approximation (GGA) of Perdew-Becke-Ernzerhof (PBE) [33] was used for the exchange-correlation function. In all calculations $FeMnO_3$ is assumed to be ferromagnetic (FM) and spin polarized though $FeMnO_3$ is known to display antiferromagnetic (AFM) ground states at around 39 K [18,19]. The AFM state is observed well below room temperature, so we assume that the energetic effect of magnetic ordering is small, and the approximation of a FM configuration should not result in significant error. A plane-wave basis set with a cutoff energy of 520 eV and Γ-centered *k*-meshes with an approximate density of 8000 *k*-points per reciprocal atom were used in all calculations. The DFT + *U* method was used to treat Fe-3d ($U_{Fe} = 4.0$ eV) and Mn-3d ($U_{Mn} = 3.8$ eV) states following the previous work [34–36]. In the bixbyite structure of $FeMnO_3$, Fe and Mn ions form fcc arrays and O occupies 3/4 of the tetrahedral sites and all octahedral sites are unoccupied. The unit cell of Mn_2O_3 bixbyite structure has 32 metal sites (80 atoms). We populate these metal sites with Fe and Mn equally and randomly and construct the computational unit cell using the special quasi-random structure (SQS) method. An SQS was generated based on a Monte Carlo algorithm implemented in ATAT [37–47] with the constraint that the pair and triplet correlation functions of the SQS are identical to those of the statistically random Fe/Mn population of cation sites at least up to the third nearest neighbor.

2.4.2. The room temperature diffusivity evaluation by ab-initio molecular dynamic (MD) simulations

In order to evaluate the Li ion diffusivity in $FeMnO_3$, we performed ab-initio molecular dynamics (MD) simulations in VASP using the SQS structure of $FeMnO_3$ consisting of 16 f.u. and a dilute amount of Li. A minimal Γ-centered 1 × 1 × 1 k-point grid was

chosen to keep the computational cost at a reasonable level after a convergence test. Our simulations were performed in the canonical ensemble using the Nose thermostat [48,49]. For each run, we used the Velocity-Verlet time integration scheme with a time step of 2 fs. To account for thermal expansion, the supercell volume was determined for each temperature by the volume where the average pressure was approximately zero based on a series of short (1 ps) runs at varying volumes [50]. In the MD simulations, the $FeMnO_3$ compound was assigned an initial temperature of 100 K. Then the system was heated up to target temperatures (600 K–1800 K) in 2 ps and equilibrated for 5 ps. The MD simulations for the diffusion were then performed for 40 ps with no sign of melting [51]. The diffusivity of each target temperature was obtained by fitting the mean square displacement over time:

$$D = \frac{1}{2t}[r(t)]^2 \quad (1)$$

where r(t) is the displacement of Li ions at time (t). D is obtained by a linear fitting to the dependence of average mean square displacement over 2t. The room temperature diffusivity was obtained by extrapolating the diffusivity values at target temperatures to room temperature based on the Arrhenius relationship. When the diffusivity values at different temperatures were collected, the activation barrier is evaluated by linear fitting of the slope of the diffusivity profile versus 1/T:

$$\ln(D) = \ln(D_0) - E_{Act}/kT \quad (2)$$

where D_0 is the temperature-independent pre-exponential. E_{Act} is the activation barrier. k is the Boltzmann constant.

3. Results and discussion

The $FeMnO_3$/graphene composite (FMO-RGO) and pure $FeMnO_3$ (FMO) were characterized by X-ray diffraction and the results are given in Fig. 1. The diffraction peaks located at $2\theta = 23.1°$, 33.0°, 38.2°, 55.2° and 65.7° are indexed as cubic $FeMnO_3$ (JCPDS card No.75-0849), without any signs of other impurity phases. The XRD diffraction patterns of FMO and FMO-RGO are virtually identical. It is worth mentioning that $FeMnO_3$ (JCPDS card No.75-0849) and α-Mn_2O_3 (JCPDS card No.71-0636) have the nearly same diffraction pattern (Fig. 1). Therefore $FeMnO_3$ has the same crystal structure as α-Mn_2O_3. That means half of the manganese atoms in α-Mn_2O_3 are substituted by iron atoms in $FeMnO_3$ without changing the crystal structure. The analysis of X-ray fluorescence spectrometer (XRF) find that the atomic ratio of Fe and Mn in FMO is 1.03: 1 (≈1: 1), further confirming the successful synthesis of FMO.

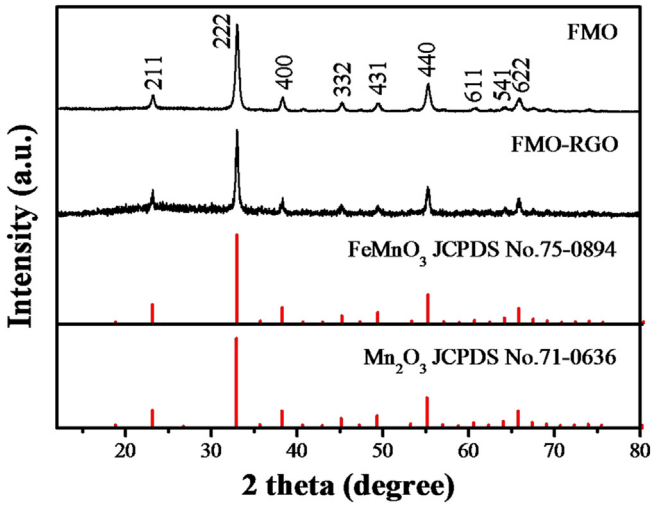

Fig. 1. XRD patterns of samples FMO and FMO-RGO.

X-ray photoelectron spectroscopy (XPS) was preformed to characterize the elemental composition and bonding configuration of FMO-RGO. Fig. 2a shows the spectrum of Fe 2p with two large peaks located at 724.6 eV (Fe $2P_{1/2}$) and 711.2 eV (Fe $2P_{3/2}$). The two minor satellite peaks next to the large peaks are due to the existence of Fe^{3+} [52]. In Fig. 2b, two characteristic peaks of Mn 2p located at 653.3 eV (Mn $2P_{1/2}$) and 641.6 eV (Mn $2P_{3/2}$) are attributed to Mn^{3+} [53] with no sign of other valence states of the manganese ions. This result is also consistent with the XRD analysis that $FeMnO_3$ was successfully synthesized (Fig. 1).

Raman spectroscopy was used for the characterization of graphene in FMO-RGO and the results are shown in Fig. 3. The two peaks at 1350 and 1590 cm^{-1}, correspond to the well-defined D band and G band of RGO, respectively. The low D/G intensity ratio ($I_D/I_G < 1$) illustrates the formation of reduced graphene oxides during the hydrothermal treatment. Two small peaks at 312 and 653 cm^{-1} are attributed to the presence of $FeMnO_3$ in FMO-RGO [54].

The pore size and surface area of the electrode materials were measured by using nitrogen adsorption–desorption isotherms (Fig. 4). The specific surface area of FMO-RGO calculated from BET is 89.65 $m^2\ g^{-1}$ which is more than twice the value (39.23 $m^2\ g^{-1}$) of FMO. The average pore size of FMO (inset of Fig. 4a) is calculated to be 16 nm using the Barrett–Joyner–Halenda (BJH) method. This type of pores is likely resulted from the aggregation of FMO particles. In FMO-RGO, in addition to the 16 nm pores, there is a distinct new type of mesopores centered at 4 nm which are possibly formed between the FMO particles and reduced graphene sheets.

From SEM images, it is apparent that FMO consists of particles with a variety of sizes and shapes (Fig. 5a). A high magnification image shown in Fig. 5b reveals that the FMO particles are made of small particles. Fig. 5c and d shows that the microstructure of FMO-RGO which consists of $FeMnO_3$ particles and graphene. In comparison with the FMO sample, graphene sheets are observed with FMO particles anchored on them (Fig. 5d). Further analysis of the TEM image in Fig. 5e reveals that the FMO particles approximately 30–40 nm in diameter are homogenously dispersed on the surface of graphene sheets. A high resolution TEM image of a single primary particle (Fig. 5f) shows the lattice fringes of the (222) plane of $FeMnO_3$, revealing the highly crystalline nature of FMO/RGO, which is confirmed by the analysis of SAED pattern shown in the inset of Fig. 5f.

Cyclic-voltammetric measurements were carried out to assess the electrochemical properties of the sample FMO-RGO (Fig. 6a). In the first cathodic sweep, two peaks are detected at around 0.55 and 1.1 V respectively. The tiny peak at 1.1 V is attributed to the reduction of Mn^{3+} to Mn^{2+} [17,55], which disappears in subsequent cycles. The sharp peak at around 0.55 V is assigned to the reduction reactions of Mn^{2+} and Fe^{3+} to their metallic states embedded in the Li_2O structure [17,55,56], which shifts at around 0.7 V in the second and third cycles. A peak attributed to the formation of a solid electrolyte interphase layer (SEI) in manganese-based oxide electrode usually at from 0.7 to 0.9 V [55,57] was not observed. It is possible that the sharp peak at 0.55 V obscured the SEI peak at adjacent voltage. In the first anodic sweep, the broad peaks at around 1.3 and 1.75 V are attributed to the oxidation reactions of Mn to MnO and Fe to Fe_3O_4, respectively [17,55,56]. In the second and third anodic sweeps, there is little change in the oxidation reaction of Mn^0 to Mn^{2+} at the peak at 1.3 V but slight changes in the oxidation reaction of Fe to Fe_3O_4 at the peak from 1.75 to 1.85 V. Moreover, a new peak appears at around 2.1 V and it becomes

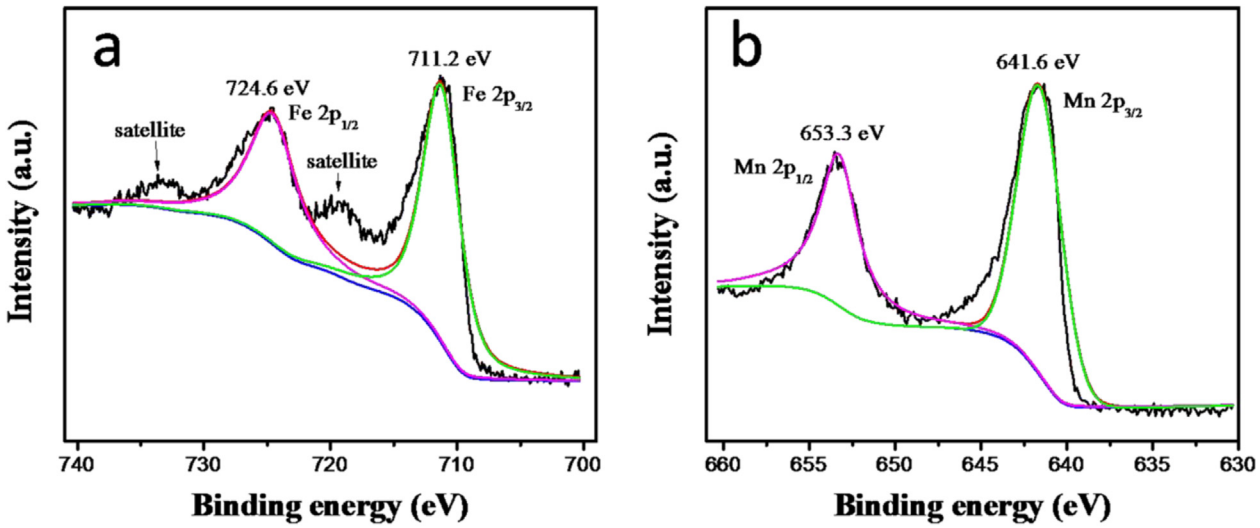

Fig. 2. (a) Fe 2p and (b) Mn 2p survey XPS spectra of FMO-RGO.

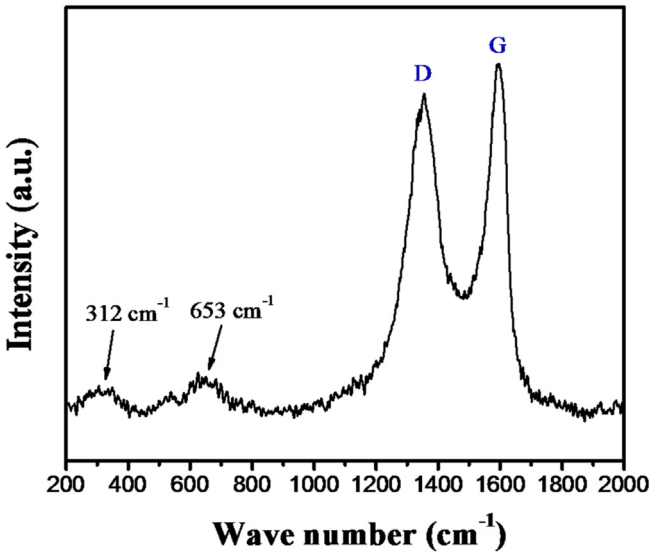

Fig. 3. Raman patterns of FMO-RGO.

strong during the discharge/charge process, indicating the occurrence of higher oxidation state of Mn [21].

The galvanostatic charge/discharge experiments were conducted to evaluate electrochemical properties of LIBs and the results are shown in Fig. 6b. The FMO-RGO based electrode shows a specific capacity of 1569.2 mAh g^{-1} in the first cycle at a current density of 200 mA g^{-1}. The electrode still displays a very high capacity of 1008.8 mAh g^{-1} even in the 100th cycles. The FMO based electrode displays a specific capacity of 1021 mAh g^{-1} in the first cycle and it decreases very quickly to only 127.4 mAh g^{-1} in the 100th cycles. This value is much lower than 1008.8 mAh g^{-1} of FMO-RGO. In order to understand the role of graphene, the electrochemical performance of mechanically mixed FMO and RGO: FMO/RGO MIX, was measured and the results are shown in Fig. 6b. The FMO/RGO MIX electrode displays a specific capacity of 1183.4 mAh g^{-1} in the first cycle and then the capacity decreases to 432.6 mAh g^{-1} in the 100th cycles. Although it is much higher than the 127.4 mAh g^{-1} of the pure FMO, the 432.6 mAh g^{-1} capacity of FMO/RGO MIX is much lower than 1008.8 mAh g^{-1} of FMO-RGO. That implies that some interfacial interactions between the FMO and RGO occurred in FMO-RGO but not in FMO/RGO MIX. Further investigation on FMO-RGO found that a specific capacity of 1155.3 mAh g^{-1} can be retained even after 300 cycles (Fig. 6c), indicating a superior reversible capacity of FMO-RGO compared to that of the previously reported transition-metal oxides such as Mn_2O_3 [8], Mn_3O_4 [9] and $CoMn_2O_4$ [15]. This good reversible capacity of FMO-RGO likely results from a combined effect of the high theoretical capacity storage of $FeMnO_3$ and the limited aggregation of active materials (since they are anchored on the graphene sheets). It is worth noting that the specific capacity increases in two stages in Fig. 6c. The increase associated with the first stage which is from 60 to 130 cycles, possibly is due to the activation process of the anode materials [55,58], and the second stage increase which begins at the 180th cycle, is probably due to the valence of manganese changes from Mn^{2+} to higher than Mn^{2+} as illustrated by others [21,59]. Moreover, the composite shows an exceptional rate performance as it can be seen that an extremely high capacity of 851.7 mAh g^{-1} at a current density of 3200 mA g^{-1} is achieved (Fig. 6d). When the current density increases from 200 mA g^{-1} to 3200 mA g^{-1} and then returns to 200 mA g^{-1}, FMO-RGO exhibits a stable capacity recovery at 1190 mAh g^{-1} and this capacity is retained upon the subsequent cycles.

Electrochemical impedance spectroscopy (EIS) plots of FMO-RGO and FMO based electrodes in the initial state and the 10th cycle state are compared in Fig. 7a and b. The semicircles in the high- and medium-frequency regions are representative of the solid electrolyte interface (SEI) resistance and the charge-transfer impedance, respectively [59]. The impedance of the FMO-RGO based electrode is much smaller than that of the FMO electrode both in the initial state and the 10th cycle, therefore FMO-RGO has better electrical conductivity than the pure $FeMnO_3$. Moreover, the impedance of FMO-RGO is stable during the charge/discharge process, which is possibly attributed to that the graphene prevents the $FeMnO_3$ particles from aggregating, but the impedance of FMO increases greatly after 10 cycles.

In an effort to further understand the properties of FMO, we use first-principles DFT calculations to predict the band gap and Li ion diffusivity of FMO. The quasi-random (SQS) structure of FMO used for the calculation is shown in Fig. 8a and Table S1. The DFT calculations show that the band structure of the FMO has “half semiconductor” features: a very small gap in one spin channel and a

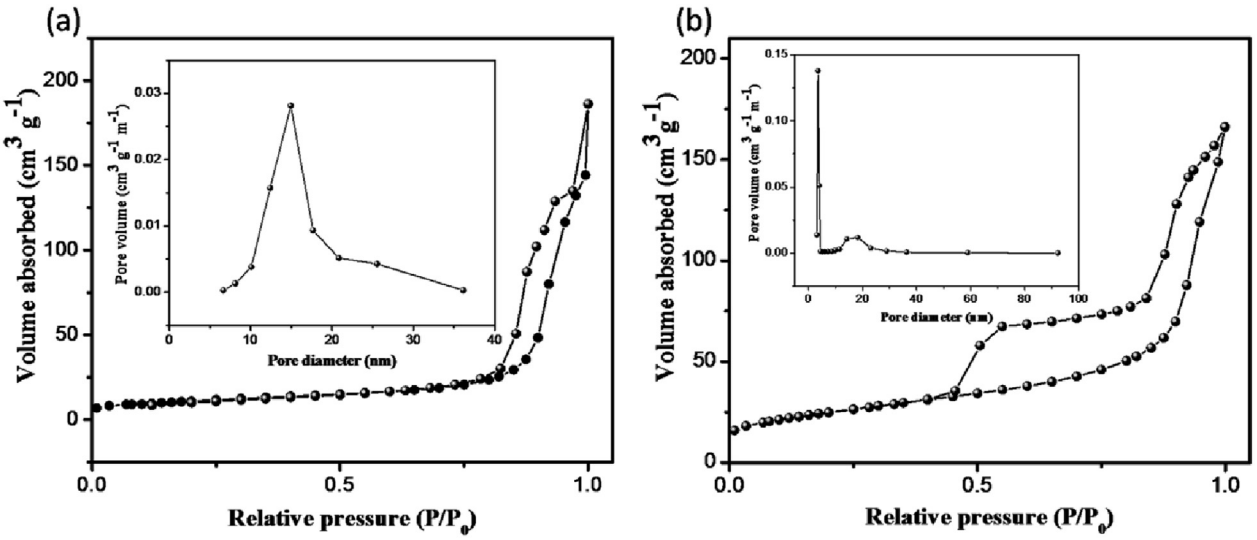

Fig. 4. N_2 absorption/desorption isotherm plot of (a) FMO and (b) FMO-RGO (pore diameter distribution curve (inset)).

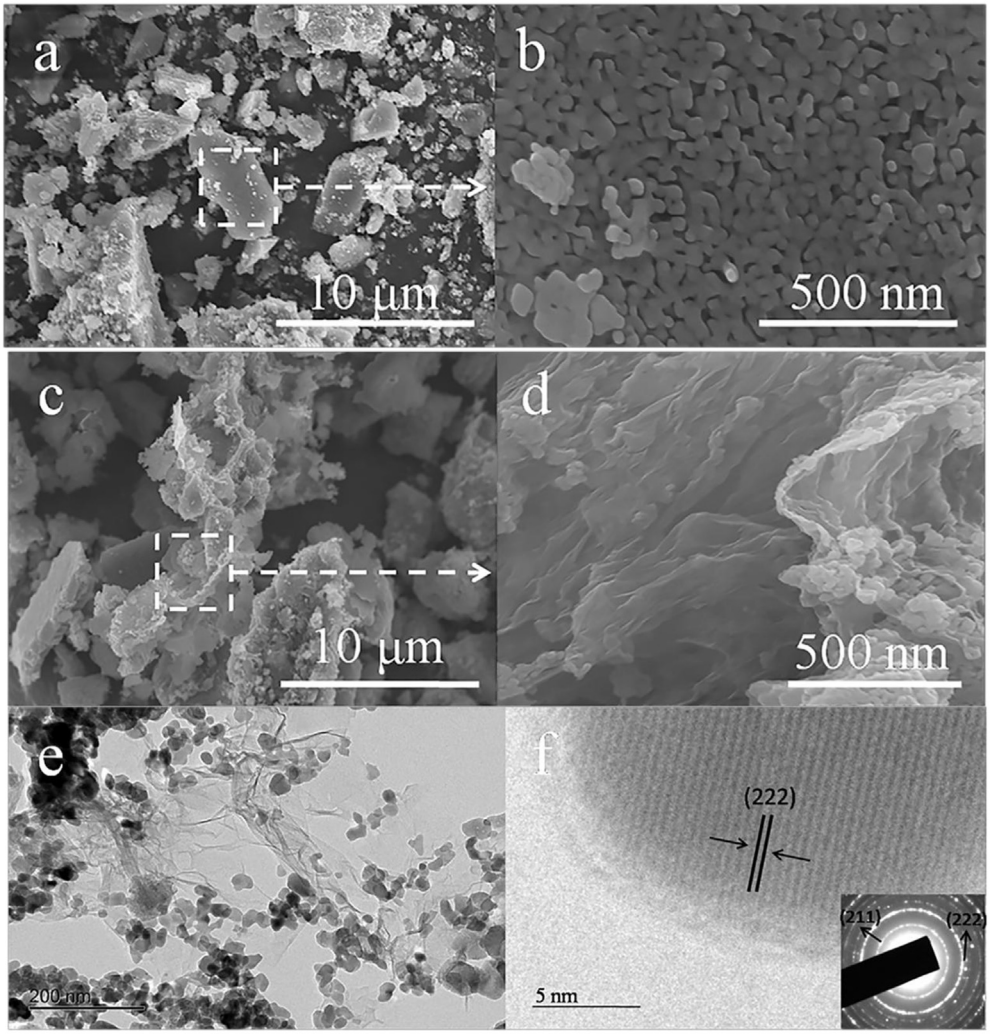

Fig. 5. SEM images of (a), (b) FMO and (c), (d) FMO-RGO. (e) TEM, (f) HRTEM and SAED (inset (f)) images of FMO-RGO.

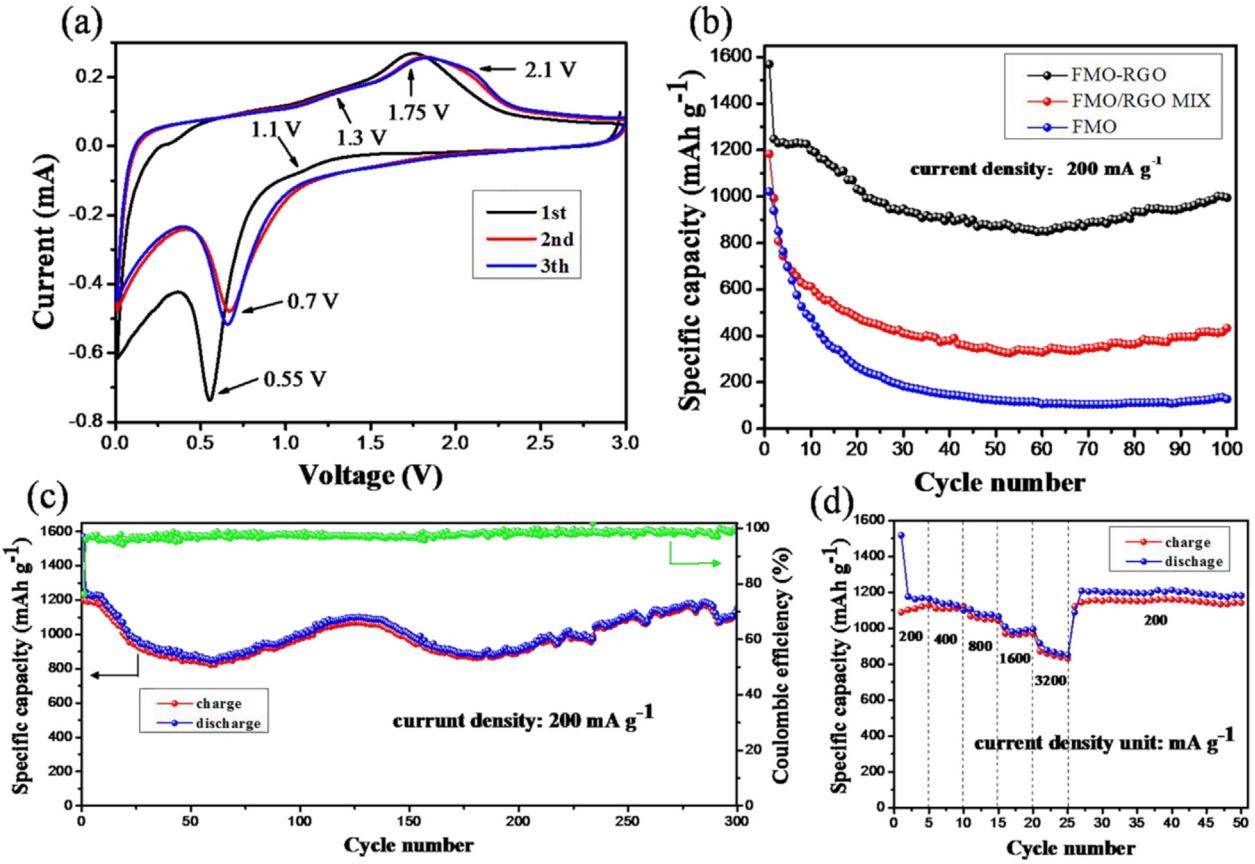

Fig. 6. (a) Cyclic-voltammograms of FMO-RGO at a scan rate of 0.5 mV s^{-1}. (b) Cycling performance of FMO-RGO, FMO/RGO MIX and FMO at a current density of 200 mA g^{-1}. (c) Cycling performance of FMO-RGO at a current density of 200 mA g^{-1} for 300 cycles. (d) Rate performance of FMO-RGO at various current densities.

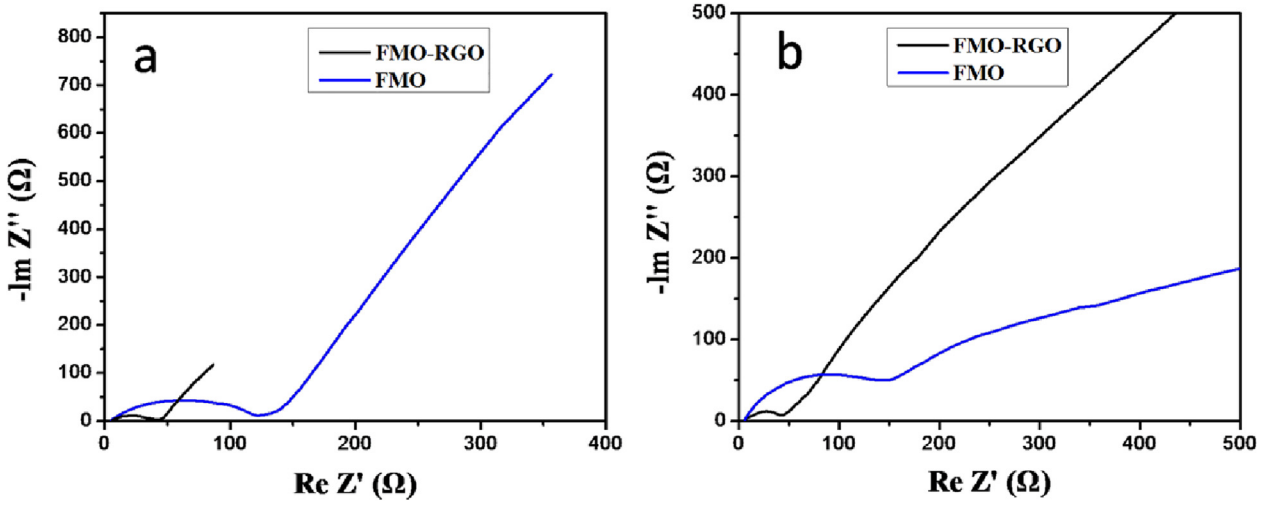

Fig. 7. (a) Initial state and (b) 10th cycle at a current density of 500 mA g^{-1} EIS results of FMO-RGO and FMO based electrode.

relatively large gap in the opposite spin channel. The small band gap around 0.3 eV (Silicon, 0.75 eV [25]) of FMO suggests it might have a good electrical conductivity (Fig. 8b). Fig. 8c shows the Arrhenius plot for the calculated diffusion coefficients at temperatures from 600 K to 1800 K. The extrapolated Li ion diffusion coefficient of FMO at room temperature is 3.9×10^{-12} cm^2 s^{-1} with an activation energy of 0.51 eV (Fig. 8c) which is comparable to most state-of-the-art high-rate electrode materials like $LiMn_2O_4$, ~10^{-11} cm^2 s^{-1} [26] and graphite, 1.12×10^{-10} cm^2 s^{-1} [27]. The calculated small band gap and high Li ion diffusivities lead to the high kinetics in the lithiation reaction and fast diffusion channels for lithium ions, which are beneficial to the performance of FMO based electrode in LIBs as reported in other materials [60]. A high specific capacity of 1021 mAh g^{-1} of the FMO based electrode in the first cycle is consistent with this calculation. As a composite electrode material of FMO-RGO, adding graphene properly to transition

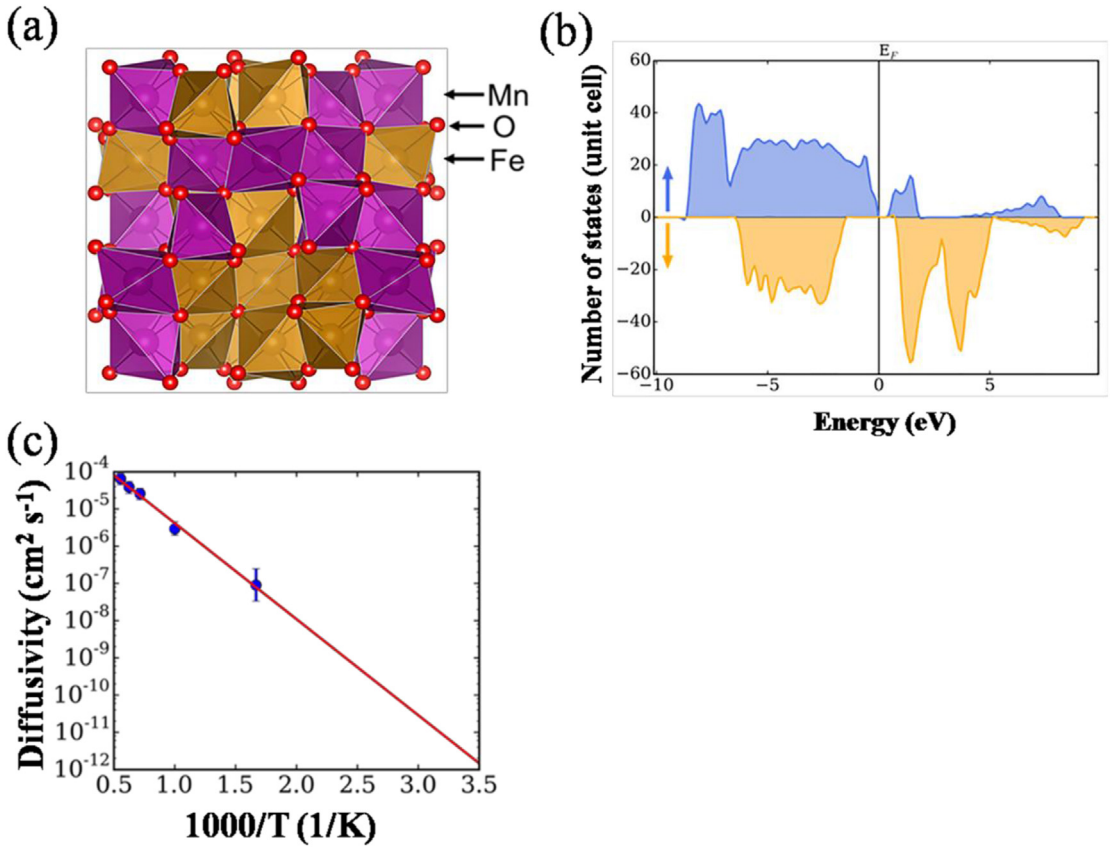

Fig. 8. (a) The disordered structure of the $FeMnO_3$ generated by the SQS method. (b) Calculated density of states for the $FeMnO_3$. (c) Arrhenius plot of the Li ion diffusion coefficient in $FeMnO_3$. The error bar corresponds to statistical uncertainty in the fitting of the mean square displacement to time curve.

metal oxide electrode material can enhance corresponding capacities and ionic conductivities by offering larger surface area and shorter Li transport path length, as evidenced by the results.

4. Conclusions

In summary, we successfully prepared $FeMnO_3$ and measured its electrochemical properties. To enhance the electrochemical performance of $FeMnO_3$, graphene was introduced to make a $FeMnO_3$/graphene composite. The resultant composite exhibited a high reversible capacity of 1155.3 mAh g^{-1} after 300 cycles at 200 mA g^{-1}, as well as a very good rate performance of 851.7 mAh g^{-1} at a current density of 3200 mA g^{-1}. This high performance is believed to be attributed to intrinsically high capacity of $FeMnO_3$, a large surface area of 89.65 m^2 g^{-1} and good electrical conductivity of the $FeMnO_3$/graphene composite. In other words, the excellent performance is due to the synergy between the intrinsic $FeMnO_3$ and the graphene sheets. Furthermore, the DFT calculations showed that $FeMnO_3$ has a small band gap (indicating the possibility of good electrical conductivity) and excellent Li ion diffusivity in $FeMnO_3$. These properties are important for an electrode. The high-performance anode material based on the $FeMnO_3$/graphene composite reported here provides us a promising anode material for LIBs.

Acknowledgements

The authors gratefully acknowledge the financial support of the National Key Research and Development Program (2016YFA0202900), the National Science Foundation of China (No. 51072117, 51672173), Shanghai Science and Technology Committee (13JC1403300), and Science and Technology Planning Project of Guangdong Province (2016A010103018).

Z.Y. and C.W. (DFT calculations) were supported as part of the Center for Electrochemical Energy Science (CEES), an Energy Frontier Research Center funded by the U.S. Department of Energy, Office of the Science, Basic Energy Science (Award No. DE-AC02-06CH11357). We gratefully acknowledge the computing resources from: 1) the National Energy Research Scientific Computing Center, a DOE Office of Science User Facility supported by the Office of Science of the U.S. Department of Energy under Contract DE-AC02-05CH11231. 2) Blues, a high-performance computing cluster operated by the Laboratory Computing Resource Center at Argonne National Laboratory.

Appendix A. Supplementary data

Supplementary data related to this article can be found at http://dx.doi.org/10.1016/j.jallcom.2016.10.249.

References

[1] J.-M. Tarascon, M. Armand, Issues and challenges facing rechargeable lithium batteries, Nature 414 (2001) 359–367.
[2] A.R. Armstrong, C. Lyness, P.M. Panchmatia, M.S. Islam, P.G. Bruce, The lithium intercalation process in the low-voltage lithium battery anode $Li_{1+x}V_{1-x}O_2$, Nat. Mater 10 (2011) 223–229.
[3] B. Dunn, H. Kamath, J.-M. Tarascon, Electrical energy storage for the grid: a battery of choices, Science 334 (2011) 928–935.
[4] A. Magasinski, P. Dixon, B. Hertzberg, A. Kvit, J. Ayala, G. Yushin, High-performance lithium-ion anodes using a hierarchical bottom-up approach, Nat. Mater 9 (2010) 353–358.
[5] L. Ji, Z. Lin, M. Alcoutlabi, X. Zhang, Recent developments in nanostructured

anode materials for rechargeable lithium-ion batteries, Energy Environ. Sci. 4 (2011) 2682–2699.
[6] X. Sun, C. Zhou, M. Xie, H. Sun, T. Hu, F. Lu, S.M. Scott, S.M. George, J. Lian, Synthesis of ZnO quantum dot/graphene nanocomposites by atomic layer deposition with high lithium storage capacity, J. Mater. Chem. A 2 (2014) 7319–7326.
[7] Y. Zhang, H. Liu, Z. Zhu, K.-W. Wong, R. Mi, J. Mei, W.-M. Lau, A green hydrothermal approach for the preparation of graphene/α-MnO_2 3D network as anode for lithium ion battery, Electrochim. Acta 108 (2013) 465–471.
[8] Y. Qiao, Y. Yu, Y. Jin, Y.-B. Guan, C.-H. Chen, Synthesis and electrochemical properties of porous double-shelled Mn_2O_3 hollow microspheres as a superior anode material for lithium ion batteries, Electrochim. Acta 132 (2014) 323–331.
[9] J. Wang, N. Du, H. Wu, H. Zhang, J. Yu, D. Yang, Order-aligned Mn_3O_4 nanostructures as super high-rate electrodes for rechargeable lithium-ion batteries, J. Power Sources 222 (2013) 32–37.
[10] H. Jiang, Y. Hu, S. Guo, C. Yan, P.S. Lee, C. Li, Rational design of MnO/carbon nanopeapods with internal void space for high-rate and long-life Li-ion batteries, ACS Nano 8 (2014) 6038–6046.
[11] N.K. Chaudhari, M.-S. Kim, T.-S. Bae, J.-S. Yu, Hematite (α-Fe_2O_3) nanoparticles on vulcan carbon as an ultrahigh capacity anode material in lithium ion battery, Electrochim. Acta 114 (2013) 60–67.
[12] X. Jiang, X. Yang, Y. Zhu, Y. Yao, P. Zhao, C. Li, Graphene/carbon-coated Fe_3O_4 nanoparticle hybrids for enhanced lithium storage, J. Mater. Chem. A 3 (2015) 2361–2369.
[13] K. Cao, L. Jiao, Y. Liu, H. Liu, Y. Wang, H. Yuan, Ultra-high capacity lithium-ion batteries with hierarchical CoO nanowire clusters as binder free electrodes, Adv. Funct. Mater 25 (2015) 1082–1089.
[14] X. Liu, J. Zhang, W. Si, L. Xi, S. Oswald, C. Yan, O.G. Schmidt, High-rate amorphous SnO_2 nanomembrane anodes for Li-ion batteries with a long cycling life, Nanoscale 7 (2015) 282–288.
[15] Y.R. Denny, K. Lee, C. Park, S.K. Oh, H.J. Kang, D.-S. Yang, S. Seo, Electronic, electrical and optical properties of undoped and Na-doped NiO thin films, Thin Solid Films 591 (2015) 255–260.
[16] Z.J. Othman, O. Hafef, A. Matoussi, F. Rossi, G. Salviati, AC conductivity and structural properties of Mg-doped ZnO ceramic, Appl. Phys. A 121 (2015) 625–634.
[17] M. Bijelić, X. Liu, Q. Sun, A.B. Djurišić, M.H. Xie, A.M. Ng, C. Suchomski, I. Djerdj, Ž. Skoko, J. Popović, Long cycle life of $CoMn_2O_4$ lithium ion battery anodes with high crystallinity, J. Mater. Chem. A 3 (2015) 14759–14767.
[18] S. Rayaprol, S. Kaushik, Magnetic and magnetocaloric properties of $FeMnO_3$, Ceram. Int. 41 (2015) 9567–9571.
[19] S. Rayaprol, S. Kaushik, P. Babu, V. Siruguri, Structure and magnetism of $FeMnO_3$, in: AIP Conf. Proc, 2013, pp. 1132–1133.
[20] H. Liu, Z. Li, Y. Liang, R. Fu, D. Wu, Facile synthesis of MnO multi-core@ nitrogen-doped carbon shell nanoparticles for high performance lithium-ion battery anodes, Carbon 84 (2015) 419–425.
[21] Y. Sun, X. Hu, W. Luo, F. Xia, Y. Huang, Reconstruction of conformal nanoscale MnO on graphene as a high-capacity and long-life anode material for lithium ion batteries, Adv. Funct. Mater 23 (2013) 2436–2444.
[22] A.K. Geim, Graphene: status and prospects, Science 324 (2009) 1530–1534.
[23] X. Yang, C. Cheng, Y. Wang, L. Qiu, D. Li, Liquid-mediated dense integration of graphene materials for compact capacitive energy storage, Science 341 (2013) 534–537.
[24] A. Zunger, S.-H. Wei, L. Ferreira, J.E. Bernard, Special quasirandom structures, Phys. Rev. Lett. 65 (1990) 353.
[25] J. Heyd, J.E. Peralta, G.E. Scuseria, R.L. Martin, Energy band gaps and lattice parameters evaluated with the Heyd-Scuseria-Ernzerhof screened hybrid functional, J. Chem. Phys. 123 (2005) 174101.
[26] M. Park, X. Zhang, M. Chung, G.B. Less, A.M. Sastry, A review of conduction phenomena in Li-ion batteries, J. Power Sources 195 (2010) 7904–7929.
[27] P. Yu, B.N. Popov, J.A. Ritter, R.E. White, Determination of the lithium ion diffusion coefficient in graphite, J. Electrochem. Soc. 146 (1999) 8–14.
[28] G. Kresse, J. Hafner, Ab initio molecular dynamics for liquid metals, Phys. Rev. B 47 (1993) 558.
[29] G. Kresse, J. Hafner, Ab initio molecular-dynamics simulation of the liquid-metal-amorphous-semiconductor transition in germanium, Phys. Rev. B 49 (1994) 14251.
[30] G. Kresse, J. Furthmüller, Efficiency of ab-initio total energy calculations for metals and semiconductors using a plane-wave basis set, Comp. Mater. Sci. 6 (1996) 15–50.
[31] G. Kresse, J. Furthmüller, Efficient iterative schemes for ab initio total-energy calculations using a plane-wave basis set, Phys. Rev. B 54 (1996) 11169.
[32] P.E. Blöchl, Projector augmented-wave method, Phys. Rev. B 50 (1994) 17953.
[33] J.P. Perdew, M. Ernzerhof, K. Burke, Rationale for mixing exact exchange with density functional approximations, J. Chem. Phys. 105 (1996) 9982–9985.
[34] S. Dudarev, G. Botton, S. Savrasov, C. Humphreys, A. Sutton, Electron-energy-loss spectra and the structural stability of nickel oxide: an LSDA+ U study, Phys. Rev. B 57 (1998) 1505.
[35] J. Chen, X. Wu, A. Selloni, Electronic structure and bonding properties of cobalt oxide in the spinel structure, Phys. Rev. B 83 (2011) 245204.
[36] J. Chen, A. Selloni, Electronic states and magnetic structure at the Co_3O_4 (110) surface: a first-principles study, Phys. Rev. B 85 (2012) 085306.
[37] E. Cockayne, A. van de Walle, Building effective models from sparse but precise data: application to an alloy cluster expansion model, Phys. Rev. B 81 (2010) 012104.
[38] A. van de Walle, Multicomponent multisublattice alloys, nonconfigurational entropy and other additions to the Alloy Theoretic Automated Toolkit, Calphad 33 (2009) 266–278.
[39] A. van de Walle, Methods for first-principles alloy thermodynamics, JOM 65 (2013) 1523–1532.
[40] A. van de Walle, A complete representation of structure-property relationships in crystals, Nat. Mater 7 (2008) 455–458.
[41] A. Van de Walle, M. Asta, Self-driven lattice-model Monte Carlo simulations of alloy thermodynamic properties and phase diagrams, Model. Simul. Mater. Sci. 10 (2002) 521.
[42] A. Van de Walle, M. Asta, G. Ceder, The alloy theoretic automated toolkit: a user guide, Calphad 26 (2002) 539–553.
[43] A. van de Walle, G. Ceder, Automating first-principles phase diagram calculations, J. Phase Equilib. 23 (2002) 348–359.
[44] A. van de Walle, D. Ellis, First-principles thermodynamics of coherent interfaces in samarium-doped ceria nanoscale superlattices, Phys. Rev. Lett. 98 (2007) 266101.
[45] A. van de Walle, Q. Hong, L. Miljacic, C.B. Gopal, S. Demers, G. Pomrehn, A. Kowalski, P. Tiwary, Ab initio calculation of anisotropic interfacial excess free energies, Phys. Rev. B 89 (2014) 184101.
[46] A. van de Walle, Q. Hong, S. Kadkhodaei, R. Sun, The free energy of mechanically unstable phases, Nat. Commun. 6 (2015).
[47] A. Van de Walle, P. Tiwary, M. De Jong, D. Olmsted, M. Asta, A. Dick, D. Shin, Y. Wang, L.-Q. Chen, Z.-K. Liu, Efficient stochastic generation of special quasirandom structures, Calphad 42 (2013) 13–18.
[48] S. Nosé, A unified formulation of the constant temperature molecular dynamics methods, J. Chem. Phys. 81 (1984) 511–519.
[49] N. Shuichi, Constant temperature molecular dynamics methods, Prog. Theor. Phys. Supp. 103 (1991) 1–46.
[50] D.E. Farrell, C. Wolverton, Structure and diffusion in liquid complex hydrides via ab initio molecular dynamics, Phys. Rev. B 86 (2012) 174203.
[51] Y. Mo, S.P. Ong, G. Ceder, First principles study of the $Li_{10}GeP_2S_{12}$ lithium super ionic conductor material, Chem. Mater 24 (2011) 15–17.
[52] T. Yamashita, P. Hayes, Analysis of XPS spectra of Fe^{2+} and Fe^{3+} ions in oxide materials, Appl. Surf. Sci. 254 (2008) 2441–2449.
[53] A.A. Audi, P. Sherwood, Valence-band x-ray photoelectron spectroscopic studies of manganese and its oxides interpreted by cluster and band structure calculations, Surf. Interface Anal. 33 (2002) 274–282.
[54] X. Niu, H. Wei, K. Tang, W. Liu, G. Zhao, Y. Yang, Solvothermal synthesis of 1D nanostructured Mn_2O_3: effect of Ni^{2+} and Co^{2+} substitution on the catalytic activity of nanowires, RSC Adv. 5 (2015) 66271–66277.
[55] P. Xiong, B. Liu, V. Teran, Y. Zhao, L. Peng, X. Wang, G. Yu, Chemically integrated two-dimensional hybrid zinc manganate/graphene nanosheets with enhanced lithium storage capability, ACS Nano 8 (2014) 8610–8616.
[56] S. Liu, J. Xie, Q. Su, G. Du, S. Zhang, G. Cao, T. Zhu, X. Zhao, Understanding Li-storage mechanism and performance of $MnFe_2O_4$ by in situ TEM observation on its electrochemical process in nano lithium battery, Nano Energy 8 (2014) 84–94.
[57] Z. Bai, N. Fan, C. Sun, Z. Ju, C. Guo, J. Yang, Y. Qian, Facile synthesis of loaf-like $ZnMn_2O_4$ nanorods and their excellent performance in Li-ion batteries, Nanoscale 5 (2013) 2442–2447.
[58] H. Wu, G. Yu, L. Pan, N. Liu, M.T. McDowell, Z. Bao, Y. Cui, Stable Li-ion battery anodes by in-situ polymerization of conducting hydrogel to conformally coat silicon nanoparticles, Nat. Commun. 4 (2013) 1943.
[59] Y. Zhong, M. Yang, X. Zhou, Y. Luo, J. Wei, Z. Zhou, Orderly packed anodes for high-power lithium-ion batteries with super-long cycle life: rational design of $MnCO_3$/large-area graphene composites, Adv. Mater 27 (2015) 806–812.
[60] Q. Li, H. Liu, Z. Yao, J. Cheng, T. Li, Y. Li, C. Wolverton, J. Wu, V.P. Dravid, Electrochemistry of selenium with sodium and lithium: kinetics and reaction mechanism, ACS Nano 10 (2016) 8788–8795.